Supporting Information

Leake *et al.* 10.1073/pnas.0806338105

SI Text

Strain Construction. The construct specifying a C-terminal YFP fusion to TatA was assembled as follows. The *tatA* gene was amplified using primers TATA5 (1) and TATAYFP1 (5′-GCGCGGATCCCGTACGCACCTGCTCTTTATCGTGG-3′) and chromosomal DNA from *E. coli* MC4100 (2) as template. After digestion with EcoRI and BamHI the product was cloned into the same sites in pBluescript SK II+ (Stratagene) to give plasmid pTatA-NOSTOP1. The *yfp* gene was amplified by using primers YFP1 (5′-GCGCGAATTCCGTACGGTGAGCAAGGGCGAG-GAGC-3′) and YFP2 (5′-GCGCGGATCCCACGTGTTACACCT-GCTCTTTATCGTTACTTGTACAGCTCGTCCATGC-3′) and plasmid pEYFP-N1 (Clontech) as template. The product was digested with EcoRI and BamHI and cloned into pBluescript SK II+ to give pYFP1. Plasmid pYFP1 was subsequently digested with BamHI and BsiWI and cloned into pTatA-NOSTOP1 that had been digested with the same enzymes to give $pTATA_{YFP}$.

Recombination of the *tatA-yfp* allele, including the *tatA* promoter region, onto the *E. coli* chromosome was achieved as follows. The *tatA* gene and *tatA* promoter region were amplified with primers TATAPROM1 (5′-GCGCGAATTCTGTCGGT-TGGCG CAAAACACGCTG-3′) and TATAYFP1 by using chromosomal DNA from strain MC4100 as template. After digestion with EcoRI and BamHI the product was cloned into the same sites in pBluescript SK II+ (Stratagene) to give plasmid pTatA-NOSTOP2. The *yfp* gene from pYFP1 was released by digestion with BamHI and BsiWI and cloned into pTATA-NOSTOP2 that had been digested with the same enzymes to give plasmid $pTATA2_{YFP}$. The *tatA-yfp* fusion allele was subsequently introduced into plasmid pRS552 (3). This was achieved by amplification of the *tatA-yfp* coding region from plasmid $pTATA2_{YFP}$ by using the primers KSB1 (5′-GCGCAGATCTCGGCCAGT-GAATTGTAATACG-3′) and KSB2 5′-GCGCAGA TCTGCTC-GAAATTAACCCTCACTAAAGG-3′), digestion with BglII, and cloning into pRS552 that had been previously digested with BamHI. The *tatA-yfp* allele was delivered onto the chromosome of strain MC4100 to produce strain AAyBC, or of Δ*tatA*Δ*tatE* strain JARV-16 (4) to produce strain AyBC, or of Δ*tatAB*Δ*tatE* strain BEAD (5) to produce strain AyC, or of Δ*tatABCD*Δ*tatE* strain DADE (6) to produce strain Ay, using methodology as described (3).

Plasmid Construction. Plasmid pFAT75BC was constructed by amplifying *tatBC* from the chromosome of strain MC4100 region with forward primer 5′-GCGCGAATTCATTAAA-GAGGA GAAATTAACCATGTTTGATATCGGTTT-TAGCGAACTGC-3′ and reverse primer 5′-GCGCAGATCTTT-CTTCAGTTTTTTCGCTTTCTGC-3′. After digestion with EcoRI and BglII the fragment was cloned into pQE60 (Qiagen) digested with the same enzymes. Subsequently $tatBC^{his}$was released from pFAT75BC by digestion with EcoRI-PvuII and cloned into EcoRI-SmaI digested pBAD18 (7) to give plasmid pBAD-BC.

pQE80-CueO codes for C-terminally hexahistidine-tagged CueO. It was constructed by amplifying the *cueO* gene from strain MC4100 by using primers 5′-ATA TCGAATTCGAATAAG-GAAATAACTAT-3′ and 5′-AGCTCAATCTTTTAGTGATG-GTGATGGTGATGTACCGTAAACCCTAACATCATC-3′, digesting the resultant product with EcoRI and BamHI and cloning into pQE80 (Qiagen) digested with the same enzymes.

Cell Preparation for Microscopy. Cells were grown in LB broth with shaking at 37°C, harvested by centrifugation, and resuspended in Mops minimal media (MM) (8). Where required chloramphenicol (50 μg/ml) was added to suppress new protein synthesis ≈1 h before the end of growth, with all subsequent washes carried out in CM buffer (50 μg/ml chloramphenicol in MM). Cells were injected into a ≈5-μl flow-cell with polylysine-coated glass coverslips as the lower surface (9). Cells were allowed to settle for 10 min, washed with excess MM or CM buffer as appropriate, incubated with a 0.1% suspension of 202-nm diameter latex microspheres (Polysciences) for 2 min to mark the coverslip, and washed with excess buffer.

Fluorescence Microscopy. We used a home-built inverted fluorescence microscope (9, 10) with a ×100 Plan Fluor 1.45 NA oil-immersion objective (Nikon) and an *xyz* nanopositioning stage (E-503.00; Physik Instrumente). Bright field used fiber-coupled tungsten-halogen illumination; laser excitation used a TEM00 plane-polarized continuous-wave 532 nm DPSS laser (Laser2000 U.K.), filtered (laser-line, 532 nm), expanded three times, and focused onto the back-focal-plane of the objective lens via a dichroic mirror (530 nm long-pass). The field width was ≈30 μm and intensity was ≈260 $W{\cdot}cm^{-2}$ (≈2.6 $kW{\cdot}cm^{-2}$ for *in vitro* measurements on surface-immobilized YFP molecules; ref. 9). A separately shuttered excitation path allowed a proportion of the laser light to be focused in the sample plane to a width ≈1 μm, intensity ≈60 $kW{\cdot}cm^{-2}$. For FRAP experiments this second path was used to bleach a cell pole for typically 0.5 s. Epifluorescence illumination from the first path was used to monitor fluorescence changes continuously. Excitation polarization was either circularized upstream of the objective lens via insertion of a quarter-wave plate or linearly s- (path 1) or p- (path 2) polarized normal to the focal plane to verify no polarization dependence on spot intensity (9). The focal plane was set at a midcell height of ≈0.5 μm from the coverslip surface. Fluorescence emission was passed through the dichroic mirror, an emission filter (580-nm band-pass), and a notch rejection filter (532 nm), and imaged at ≈50 nm per pixel in frame-transfer mode at 25 Hz by a 128 × 128-pixel, cooled, back-thinned electron-multiplying CCD camera (iXon DV860-BI; Andor Technology).

Detection of Fluorescent Spots in Cells. Nonfluorescence bright-field images were acquired for each field of view of immobilized cells at a focal height of 100 nm from the coverslip surface, generally resulting in a distinct dark perimeter marking the interface between cell body and surrounding solution. Custom-written pattern recognition software (LabVIEW 8.1; National Instruments) was applied to identify these boundaries based on tolerance-limited searches for 2D cell-like shapes consisting of a rectangle of variable length capped by width-matched semicircles of variable diameter 0.5–1.5 μm, with total end-to-end length range 1.5–3.5 μm and of arbitrary long-axis rotational orientation relative to the CCD camera axes. These vital statistics were then used to create an image mask around each cell for subsequent fluorescence image analysis padding each cell perimeter by a border 300 nm wide. An initial guess for the position of fluorescent spots on each masked fluorescence image frame was made by using automated custom-written software based on a commercial Danielsson distance map algorithm (ref. 11; LabVIEW). The software searched for distinct radially symmetrical circular intensity distributions of width 100–350 nm. A circular region of interest (ROI) of radius 8 pixels was then drawn around each spot. The intensity distribution of each spot was modeled as a central Gaussian function (the complex component) plus a planar uniform component due to a combination of cellular autofluorescence, noncellular background noise, and diffusing TatA-YFP not

bound in distinct spot complexes (membrane component) specifically as follows:

1. We applied a circular mask for the contribution of the TatA-YFP complex of radius 5 pixels to the ROI, centered on the current complex centroid.
2. We multiplied pixel intensities within the circular mask by a radially symmetrical 2D Gaussian mask of fixed half-width (SD) 150 nm, and generated a revised estimate for the complex centroid weighted by this mask (9, 12).
3. We iterated steps 1 and 2 either 10 times or until the circular mask began to clip the side of the original ROI, resulting in a final centroid precision of ≈2–40 nm depending on the brightness of the spot. A 2D radially symmetrical Gaussian fit was then performed on the complex intensity component optimizing for amplitude and width.
4. We defined the total background intensity as the mean pixel intensity within the ROI but external to the final circular mask. We defined the complex intensity $I(t)$ as the sum of all pixel values within the circular mask after subtraction of the total background intensity from each pixel value.
5. We defined the instrumental component of background (the intensity not associated with cells) as the mean pixel intensity in a circular ROI, radius 8 pixels, containing no cells. Steps 1–5 were performed separately for each image.
6. We defined the cellular autofluorescence component of background as the mean pixel intensity minus the instrumental background from 12 circular ROIs, radius 8 pixels located in the cylindrical region at the periphery of the cell (i.e., centred over a segment of cell membrane), from 12 separate cells of the non-YFP parental strain (ABC).
7. We defined the membrane component of background (due to a diffusing pool of TatA-YFP not detected as distinct spots of fluorescence) for each image as the total background intensity minus the instrumental component (step 5) and the autofluorescence component (step 6).

To characterize photobleaching for the YFP component *in vivo*, an average normalized photobleach trace was first constructed to correct for differences in TatA-YFP content. Each intensity versus time trace (taken from the start of fluorescence excitation) for each long-lasting track (≥25 consecutive data points) of the AyBC strain was fit with a single exponential decay and normalized by using the preexponential factor. Normalized traces were then piled up and mean values calculated at each time abscissa. This could be fit by a single exponential decay function with bleach time constant 8.0 ± 1.0 s (± SD., using 85 tracks from different cells; Fig. S1*A*). For the non-YFP parental cell strain ABC the autofluorescence component did not have the broad heterogeneous intensity distribution observed for the AyBC strain, and thus did not need to be normalized in advance. The mean photobleach curve was fit by a double exponential decay function (Fig. S1 *A* and *B*) with bleach time constants 4.4 ± 0.9 s and 0.6 ± 0.3 s (from 12 ROIs in 12 different cells).

Defining Spots Tracks. The properties of each detected spot were then compared with those detected in the subsequent image frame. If the nearest detected spot to a previous spot position met all of the following criteria it was deemed to be the same spot and to therefore constitute a track:

1. The new spot position must be <250 nm distance from the previous position (a large enough distance so as not to bias tracking toward small displacements).
2. The spot intensity must not change by more than a factor of 2 (permitting potential continuous tracking of spots containing two photoactive YFP molecules in the previous frame but only one in the next).
3. The fitted Gaussian width must not change by more than a factor of two (permitting continuous tracking of defocus-broadened spots within the focal imaging depth).

If all these conditions are satisfied the spot location is recorded as belonging to the same track as in the previous frame (each unique track consisting of an array recording time, *xy* coordinates relative to the camera reference axes, width and intensities), if not then the previous track is terminated. If two separate tracks are <250 nm distance from each other then both are terminated. In subsequent analysis, only tracks consisting of at least five consecutive image frames were used.

Coordinate Transformation of Spot Locations. The positions of spots were recorded in the Cartesian coordinate system of the camera reference frame. However, movement of spots was consistent with diffusion over a cell membrane surface, because tracks were observed to map out the borders of the cell for epifluorescence excitation when focusing at midcell height from the coverslip surface and the corresponding frame-averaged images had a fluorescence halo around the cell perimeter. Therefore it was necessary to transform into the coordinate system appropriate for each particular cell to consider any observed displacements as being solely in the same plane as the membrane. To achieve this, each spot in each frame was first assigned into one of three zones based on the vital-statistics of its corresponding cell: either one of two hemispherical caps or one cylindrical region. The Cartesian *xy* coordinates were then transformed into *x'y'* curvilinear coordinates based either on spherical or cylindrical polars as appropriate:

1. Define an origin (x_0,y_0) at junction of the leftmost hemispherical cap region and cylindrical region intersecting with long-axis of cell (Fig. S1*C*).
2. Rotate Cartesian camera axes so that *x*-axis is parallel to long-axis of cell:

$$x_{rot} = (x - x_0)\cos\theta + (y - y_0)\sin\theta$$

$$y_{rot} = (y - y_0)\cos\theta - (x - x_0)\sin\theta.$$

3. (*i*) If $x_{rot}<0$ OR $x_{rot}>L$ (i.e., the spot is in one of the hemispherical cap regions)

$$r' = \sqrt{(x_{rot} - x_{rot,offset})^2 + y_{rot}^2}$$

$$\phi = \sin^{-1}((x_{rot} - x_{rot,offset})/r')$$

$$x' = r'\,\phi + x_{rot,offset}.$$

And then transform:

$$z' = \sqrt{r^2 - x_{rot}^2 - y_{rot}^2}$$

$$\chi = \cos^{-1}(z'/r)$$

$$y' = r\chi.$$

Such that $x'_{offset} = 0$ for $x_{rot} < 0$ OR $x'_{offset} = L$ for $x_{rot} > L$.
(*ii*) If $0 \le x_{rot} \le L$ (i.e., the spot is in the cylindrical region):

$$z' = \sqrt{r^2 - y_{rot}^2}$$

$$\chi = cos^{-1}(z'/r)$$

$$y' = r\chi$$

$$x' = x_{rot}.$$

To avoid confusion due to the symmetry above and below the focal plane, a given track was partitioned into two separate tracks if it crossed the focal plane.

Estimation of Average Number of Spots per Cell. The number of tracks commencing from the start of each photobleach during continuous epifluorescence excitation at the 25-Hz frame rate was estimated for each cell, giving a mean of 1.8 ± 1.1 (± SD, using 121 cells) observed tracks per cell per frame for the AyBC strain. The depth of field for typical yellow spectral emissions was estimated to be 380 ± 20 nm (10), consistent with theoretical predications. Modeling the cell as a cylinder of length 2 μm, diameter 1 μm, capped at either end with 1 μm diameter hemispheres (9) indicates that the depth of field encapsulates 12.4 ± 0.7% of the membrane surface, indicating a mean total number of spots per cell of 14.5 ± 8.8 for the AyBC strain.

Estimation of TatA-YFP Number in Tracked Complexes. Estimation of TatA-YFP stoichiometry in tracked spots used a method based on the stepwise photobleaching of YFP (22). We calculated the pairwise differences for all intensity traces $I(t)$ recorded for each individual cell:

$$\Delta I_{ij} = I(t_i) - I(t_j)$$

for all data pairs for which the time $t_i > t_j$. The pairwise differences for all tracks recorded for each separate cell were then combined. The distribution of these combined pairwise differences (pairwise difference distribution function) was calculated by using 3,000 bins and normalized by the total number of pairwise differences, $n(n-1)/2$, where n is the number of data points in each trace (13). We then calculated the single-sided power spectrum from each pairwise displacement histogram. Peak detection in the power spectrum was automated by using commercial code (LabView 8.1; National Instruments) with the unitary step peak taken as that detected at the highest spatial frequency in each trace (14). A peak detection threshold was taken as four standard deviations above the high spatial frequency noise floor (defined as the standard deviation of the power spectrum signal between S_{fmax} and $S_{fmax}/2$, where S_{fmax} is the maximum spatial frequency for the power spectrum) equivalent to a probability confidence level of $P < 0.001$. The corresponding value of spatial frequency was inverted to give the characteristic "unitary step size" I_{YFP} in terms of intensity counts (typically ≈800 counts).

Each individual intensity trace for both membrane and complex components was then fitted by a single exponential decay function $I(t) = I_0\exp(-t/t_0)$, constraining t_0 to the mean YFP bleach time constant of 8.0 ± 1.0 s as measured previously. The number of TatA-YFP molecules associated with each diffusing complex was then estimated as the initial intensity of the complex component $I^C{}_0$ before any photobleaching divided by I_{YFP}. Similarly, the mean pixel count for the membrane TatA-YFP component was calculated for each track as the initial intensity of the membrane component per pixel (after subtracting the autofluorescence contribution and instrumental background) $I^M{}_0$ divided by I_{YFP}. Strains that did not possess all three essential Tat components generally had a diffuse halo appearance in epifluorescence, although some dim granular features within this halo could be seen on individual frames which were sometimes but rarely detected by the automated tracking algorithm. However, the reliability for tracking the same dim spot against a fast-moving background of other dim spots was poor when the relative number of background spots was high. FRAP experiments were performed on the Ay strain to decrease the number of background spots by photobleaching a cell pole and tracking the dim spots into the bleached area. However, because prebleaching using FRAP results in an artifactually lower estimate for membrane content, estimations of $I^M{}_0$ in these deletion strains were made in the same way as for the autofluorescence intensity of the non-YFP parental strain ABC. For all strains this was multiplied by 3,700 ± 500 pixels for cell-surface area (9) to estimate the total TatA-YFP content not associated with distinct spots, and the mean was calculated across all cells analyzed for each different cell strain. The total average TatA-YFP component associated with spots was approximated by multiplying the median value of TatA-YFP stoichiometry per complex for each cell strain by the mean number of tracks observed per frame multiplied by the appropriate correction factor for the proportion of the cell membrane being imaged in the relevant fluorescence excitation mode (12.4 ± 0.7%). The results for the cell strains used in this study are shown in Table S2.

Characterization of Cell Culture Variation and Periodicity in Stoichiometry. To assess culture-to-culture variability in the average stoichiometry of TatA-YFP complexes we performed the same quantitative analysis as before but treated data from different cultures of the same AyBC strain separately. Using data from 10 separate cell cultures we find that the general shape of the stoichiometry distribution is broadly conserved although the variation in the median estimated TatA-YFP content per complex is ≈15% (Fig. S1*D*).

To measure any periodic features to this stoichiometry we generated the pairwise difference distribution function and subsequent power spectrum from each relevant histogram (Fig. S1*E*). Across all of the different AyBC cell cultures we observe a significant peak in the range of three to five molecules for each culture, with the peak of the mean power spectrum from all cultures at 4.3 ± 0.6 TatA-YFP molecules, indicating average periodicity to the TatA-YFP complex stochiometry in multiples of about four molecules.

Testing Detection Performance Using Simulations. To test detection performance of the autotracking software we simulated single point spread functions as a radial symmetric Bessel function of FWHM width 300 nm whose amplitude was scaled to generate a total intensity at some given multiple of a typical unitary YFP brightness I_{YFP} of ≈800 counts. These were placed on a Gaussian-noise background simulated at the same level as experimental data of ≈50 counts per pixel. These simulated images were then run through the autodetection and localization algorithms recording the number of times the simulated spot was detected successfully within a 5-pixel radius of the true center, and when successfully detected the distance between the estimated centroid and the true centroid. 100 trials were made at each equivalent level of spot brightness over the range 0.5–64 equivalent YFP molecules per spot, allowing assessment of both probability of detection and localization precision (Fig. S1 *F* and *G*).

This indicates the sensitivity of detection under typical experimental conditions is 2.0 ± 0.3 YFP molecules (as defined by the point at which the detection probability equals 50%). Tests performed on the non-YFP parental cell strain ABC indicated rare detection of short-lived, dim tracks for which the spot intensity was ≈1,300 counts. This is equivalent to ~1.6 I_{YFP} units under our exposure and excitation intensity conditions and is consistent with our simulated sensitivity estimate of about two YFP molecules per spot. At the median average of spot brightness for the AyBC strain (≈25 YFP molecules) the localization precision is ≈4 nm.

Estimating the Likelihood for Mistakenly Detecting Two Diffusing Spots as One. The probability that two separate spots are erroneously detected as a single spot is estimated on the basis that that there are two principal types of "double" spot:

Type I: Those present at the start. For each complex that is visible, the probability that a given other complex is within ≈5 pixels of each other is Ares/Acell, where Ares is the psf spot area (≈20 pixels^2) and Acell is the effective pixel area of the whole cell membrane surface of ≈3,700 pixels^2 (9). With N-1 other complexes, the probability that a given visible complex is part of a double is then (N-1)Ares/Acell. Taking N as ≈15 this implies ≈7% are this sort.

Type II: Those caused by colliding. We estimate 5 in 659 tracks from 10 sampled movies, indicating <1% are this sort of double.

The total (sum of type I and type II) is therefore <8%.

Estimation of Diffusion Coefficients. Having transformed from Cartesian (xy) to the relevant curvilinear coordinates ($x'y'$) the MSD for a track of N consecutive image frames at a time interval $\tau = n\Delta t$ was defined according to (15):

$$MSD(\tau) = MSD(n\Delta t)$$

$$= \frac{1}{N-1-n} \sum_{i=1}^{N-1-n} \{[x'(i\Delta t + n\Delta t) - x'(i\Delta t)]^2$$

$$+ [y'(i\Delta t + n\Delta t) - y'(i\Delta t)]^2\}.$$

The micro diffusion coefficient was based only on a linear fit of the MSD versus τ trace (slope D) for $\tau \leq 4\ \Delta t$, where Δt is the image frame time of 40 ms (16).

In the present investigation we found that most tracks had a goodness-of-fit for a straight line to the MSD relation of correlation coefficient (R^2) > 0.8, indicating putative normal Brownian diffusion. However, some spots showed qualitative evidence for confined diffusion in the cell membrane into zones of 100- to 200-nm diameter (Fig. 3*A*), but the relatively short length of tracks in our present study did not permit conclusive statistical confirmation of this.

Modeling Translational Diffusion of TatA Complexes. We modeled translational diffusion of the TatA complex in the cytoplasmic membrane as that due to a cylinder of radius r and height h constrained two-dimensionally in a lipid bilayer bounded on one side by periplasm and on the other by cytoplasm (Fig. 3*C*). We considered two different approaches, one using modifications of the Saffman-Delbrück equations (17, 18), the other using a heuristic $1/r$ Stokes-like treatment in which the translational diffusion coefficient D varies inversely with the radius of the cylinder r (19). In both, D is given by the standard Einstein-Stokes relation of $D = kT/\lambda$ at an absolute temperature, where k is Boltzmann's constant and λ the translational frictional drag coefficient. For the Saffman-Delbrück approach λ is given by (18):

$$\lambda = 4\pi(\mu_1 + \mu_2)r\Lambda(\varepsilon) = 8\pi\eta_c r\Lambda(\varepsilon).$$

We assume the viscosities of the periplasm and cytoplasm (μ_1 and μ_2, respectively) are approximately the same, η_c. The dimensionless parameter ε is given by:

$$\varepsilon = (r/h)(\mu_1 + \mu_2)/\eta_m = 2r\eta_c/h\eta_m.$$

The viscosity of the lipid bilayer is given by the parameter η_m. We used representative values of 0.001 and 0.1 Pa.s for η_c and η_m, respectively based on previous experimental investigations of translational diffusion of a protein complex in the bacterial cytoplasmic membrane (19). The parameter Λ was previously approximated in ref. 17 but here we use the complete formulation as developed in ref. 18:

$$\Lambda(\varepsilon) = \{\varepsilon(\ln(2/\varepsilon) - \gamma + 4\varepsilon/\pi - \varepsilon^2\ln(2/\varepsilon)/2 + O(\varepsilon^2))\}^{-1}.$$

Here γ is Euler = Mascheroni constant (i.e., ≈0.5772).

For the heuristic *1/r* model:

$$\lambda = 4\pi\eta_m hr/\beta.$$

Here β is a characteristic length parameter related to the local mechanical properties of the lipid bilayer, with previous investigations indicating a plausible range of 0.5 to 500 nm to account for the observed membrane mobility data of several different protein complexes (19).

To estimate r we tried two different regimes of spatial distribution for identical protein subunits (each with cross-sectional radius r_0) within the cylinder. We approximated in both cases the cylinder height h as 3 nm based on sequence information for the transmembrane helix of the TatA monomer (20). In the disk model we approximated the spatial distribution as being approximately uniform through the circular cross-section of the cylinder, as given by:

$$\pi r_{disc}^2 \approx S.\pi r_0^2$$

$$\therefore r_{disc} \approx r_0\ \sqrt{S}.$$

The subunit stoichiometry in the complex is given by the parameter S. For the ring model we approximated the spatial distribution of protein subunits through a cross-section of the cylinder as located around the circumference of a ring such that:

$$2\pi r_{ring} \approx S.2r_0$$

$$\therefore r_{ring} \approx r_0 S/\pi.$$

We then performed a least-squares fit on the binned experimental data relating diffusion coefficient to TatA complex stoichiometry, varying the cylinder radius parameter and, for the $1/r$ model, optimizing against the length parameter β. To assess goodness-of-fit we constructed the χ^2 statistic for which the number of degrees of freedom v were taken as the number of binned datapoints D_{bin} (eight in this instance) minus the number of unconstrained parameters in the model (either one or two, since others components were fixed):

$$\chi^2 = \sum_{i=1}^{8} (D_{theory,i} - D_{bin,i}/\sigma_i)^2.$$

Here σ_i is the measurement standard deviation for diffusion coefficient for bin i. The χ^2 value for each fit was then converted to a fitting confidence probability p testing the null hypothesis that χ^2 is less than the corresponding theoretical χ^2 statistic for v degrees of freedom.

For the Saffman-Delbrück approach this indicated a moderate fit ($P = 0.84$) for the ring model with a subunit radius of 4.7 ± 1.6 nm, and a significantly worse fit for the disk model ($P = 0.43$) with a subunit radius of 11.0 ± 3.2 (Fig. S1*H*, blue fits).

Fitting the log-log data with a straight line gave an excellent fit (Fig. S1*H*, red fit) indicating a gradient of -1.2 ± 0.4 and P = 0.98. To within experimental error this is therefore consistent with the heuristic $1/r$ ring model since this predicts a gradient of −1, as opposed to the heuristic $1/r$ disk model, which predicts a gradient of -0.5.

For the Saffman-Delbrück approach a radius of 4.7 nm for a TatA-YFP monomer cannot be reconciled with the known structural data of TatA (20). An upper limit is that a monomer consists of a TatA transmembrane helix of radius ≈0.8 nm protruding perpendicular to the cytoplasmic membrane joined to an ampipathic helix of length ≈3.5 nm (21) would indicate a monomer radius if ≈2.3 nm. If free rotation of the transmembrane helix occurs this would indicate an effective radius of ≈4.6 nm. However, it is not obvious how this scheme would fit with available structural data nor how this would be integrated into a scheme for substrate translocation. The data could be fit equally well by constraining the monomer radius at 2.6 nm then reducing the membrane viscosity (≈3-fold), or increasing the cytoplasmic viscosity (≈3-fold), or decreasing the membrane thickness (≈2-fold) or combining all these types of change (e.g., if the parameters above have equal

scaling factors of ≈1.5-fold). In all cases, it was only the ring model that gave acceptable fits.

However, our results indicate significantly better agreement to a heuristic 1/*r* treatment than the Saffman-Delbrück approximations, consistent with an earlier finding (19). Considering a physically realistic subunit radius in the range 0.2 to 1.0 nm in the ring model for the 1/*r* treatment, based on the assumption that a single transmembrane helix has an effective diameter of ≈0.4 nm, indicates a characteristic length parameter of ≈0.5–1.0 nm, consistent with the low end of the range of previous findings (19).

Estimation of Cytoplasmic Content of TatA-YFP. The cytoplasmic content of TatA-YFP within each cell was estimated from measurement of the fluorescence intensity distribution profile within each cell to give independent single-cell validation of the bulk biochemical results from subcellular fractionation studies.

1. The mean spatial distribution of TatA-YFP was first approximated from the frame-averaged image of a cell by using the first 200 image acquisition frames.
2. The average intensity profile across the cell $I(y')$ was measured by calculating the mean from a 10-pixel section either side of a line passing through the cell's midpoint and perpendicular to its long-axis i.e., parallel to the y'-axis and passing through $x' = l/2$ (Fig. 4*A*) for the frame-averaged image, generating a roughly symmetrical bimodal curve with the two peaks centered on the peripheries of the cell, consistent with TatA-YFP fluorescence in the cell membrane either side of its midpoint. This is to be compared with the average intensity profile (mean profile taken from 10 separate cells) measured from the non-YFP parental strain ABC, which is much shallower and has single broad peak centred over the cell's midpoint consistent with the presence of autofluorescence components in the cytoplasm (Fig. 4*C*).
3. This average autofluorescence $I_{AF}(y')$ was modeled as a single Gaussian function centred on the cell's midpoint $y' = 0$ of width $(c_1) \approx 0.5\ \mu$m, amplitude $(\alpha_{AF}/c_1\sqrt{2\pi}) \approx 20$ counts per pixel:

$$I_{AF}(y') = \frac{a_{AF}}{c_1\sqrt{2\pi}} \exp\left(\frac{-y'^2}{2c_1^2}\right).$$

4. The average spatial distribution of cytoplasmic TatA-YFP $I_{cyt}(y')$ was assumed to be roughly the same as the average cytoplasmic autofluorescent components, and so the associated fluorescence was modeled as a multiple α of $I_{AF}(y')$:

$$I_{cyt}(y') = \alpha I_{AF}(y')$$

5. The TatA-YFP fluorescence in each membrane segment included in the profile section $I_{mem}(y')$ was modeled as the sum of two Gaussian functions of widths (c_2 and c_3) ≈0.15 μm (equivalent to full-width at half-maximum of ≈0.3 μm, identical to the point spread function width of our microscope):

$$I_{mem}(y') = \sum_{i=2}^{3} \frac{a_i}{c_i\sqrt{2\pi}} \exp\left(\frac{-(y'-b_i)^2}{2c_i^2}\right),$$

so that:

$$I = I_{mem}(y') + I_{cyt}(y') + I_{AF}(y')$$

$$= \sum_{i=1}^{3} \frac{a_i}{c_i\sqrt{2\pi}} \exp\left(\frac{-(y'-b_i)^2}{2c_i^2}\right),$$

such that:

$$a_1 = a_{AF}(1+\alpha) \text{ and } b_1 = 0.$$

6. A fit was then performed optimizing for the heights (a_2 and a_3) and positions (b_2 and b_3) of the TatA-YFP membrane fluorescence Gaussian functions, and for the cytoplasmic TatA-YFP fluorescence multiplying factor (α), limited to data points acquired from the cell's image mask i.e., one point spread function width either side of the cell boundary.
7. Total membrane and cytoplasmic TatA-YFP fluorescence contributions across the profile, S_{mem} and S_{cyt} respectively, were taken as the integrals:

$$S_{mem} = \int_{-\infty}^{+\infty} I_{cyt}dy' = \alpha a_{AF}$$

$$S_{cyt} = \int_{-\infty}^{+\infty} I_{mem}dy' = a_2 + a_3.$$

8. The relative (%) cytoplasmic TatA-YFP content (R_{cyt}) for a given cell was then taken as:

$$R_{cyt} = 100S_{cyt}/(S_{cyt} + S_{mem}) = 100\alpha a_{AF}/(a_2 + a_3).$$

Mean R_{cyt} values were then calculated from 10 separate cells for each cell strain. In the example cell shown from the Ay strain (Fig. 4*C*) $R_{cyt} = 5.1 \pm 2.0\%$. This is to be compared with the mean value taken across all strains used in the study (Table S2) of $3.3 \pm 2.5\%$, indicating that on average in excess of 95% of TatA-YFP was present in the cell membrane.

1. Sargent F, *et al.* (1998) Overlapping functions of components of a bacterial Sec-independent protein export pathway. *EMBO J* 17:3640–3650.
2. Casadaban MJ, Cohen SN (1979) Lactose genes fused to exogenous promoters in one step using a Mu-*lac* bacteriophage: *in vivo* probe for transcriptional control sequences. *Proc Natl Acad Sci USA* 76:4530–4533.
3. Simons RW, Houman F, Kleckner N (1987) Culture medium for enterobacteria. *Gene* 53:85–96.
4. Sargent F, Stanley NR, Berks BC, Palmer T (1999) Sec-independent protein translocation in *Escherichia coli*: A distinct and pivotal role for the TatB protein. *J Biol Chem* 274:36073–36083.
5. Lee PA, Buchanan G, Stanley NR, Berks BC, Palmer T (2002) Truncation analysis of TatA and TatB defines the minimal functional units required for protein translocation. *J Bacteriol* 184:5871–5879.
6. Wexler M, *et al.* (2000) TatD is a cytoplasmic protein with DNase activity. No requirement for TatD family proteins in sec-independent protein export. *J Biol Chem* 275:16717–16722.
7. Guzman LM, Belin D, Carson MJ, Beckwith J (1995) Tight regulation, modulation, and high-level expression by vectors containing the arabinose PBAD promoter. *J Bacteriol* 177:4121–4130.
8. Neidhardt FC, Bloch PL, Smith DF (1974) Culture medium for enterobacteria. *J Bacteriol* 119:736–747.
9. Leake MC, *et al.* (2006) Stoichiometry and turnover in single, functioning membrane protein complexes. *Nature* 443:355–358.
10. Lo C-J, Leake MC, Pilizota T, Berry RM (2007) Nonequivalence of membrane voltage and ion-gradient as driving forces for the bacterial flagellar motor at low load. *Biophys J* 93:294–302.
11. Danielsson PE (1980) Euclidean distance mapping. *Computer Vision Graphics Image Understanding* 14:227–248.
12. Thompson RE, Larson DR, Webb WW (2002) Precise nanometer localization analysis for individual fluorescent probes. *Biophys J* 82:2775–2783.
13. Kuo SC, Gelles J, Steuer E, Sheetz MP (1991) A model for kinesin movement from nanometer-level movements of kinesin and cytoplasmic dynein and force measurements. *J Cell Sci* 14:135–138.
14. Svoboda K, Schmidt CF, Schnapp BJ, Block SM (1993) Direct observation of kinesin stepping by optical trapping interferometry. *Nature* 365:721–727.
15. Gross DJ, Webb WW (1988) Cell surface clustering and mobility of the liganded LDL receptor measured by digital video fluorescence microscopy. *Spectroscopic Membrane Probes II*, ed Loew LM (CRC, Boca Raton, FL), pp 19–45.
16. Kusumi A, Sako Y, Yamamoto M (1993) Confined lateral diffusion of membrane receptors as studied by single-particle tracking (nanovid microscopy). Effects of calcium-induced differentiation in cultured epithelial cells. *Biophys J* 65:2021–2040.

17. Saffman PG, Delbruck M (1975) Brownian motion in biological membranes. *Proc Natl Acad Sci USA* 72:3111–3113.
18. Hughes BD, Pailthorpe BA, White LR (1981) The translational and rotational drag on a cylinder moving in a membrane. *J Fluid Mech* 110:349–372.
19. Gambin Y, *et al.* (2006) Lateral mobility of proteins in liquid membranes revisited. *Proc Natl Acad Sci USA* 103:2098–2102.
20. Gohlke U, *et al.* (2005) The TatA component of the twin-arginine protein transport system forms channel complexes of variable diameter. *Proc Natl Acad Sci USA* 102:10482–10486.
21. Porcelli I, *et al.* (2002) Characterization and membrane assembly of the TatA component of the *Escherichia coli* twin-arginine protein transport system. *Biochemistry* 41:13690–13697.

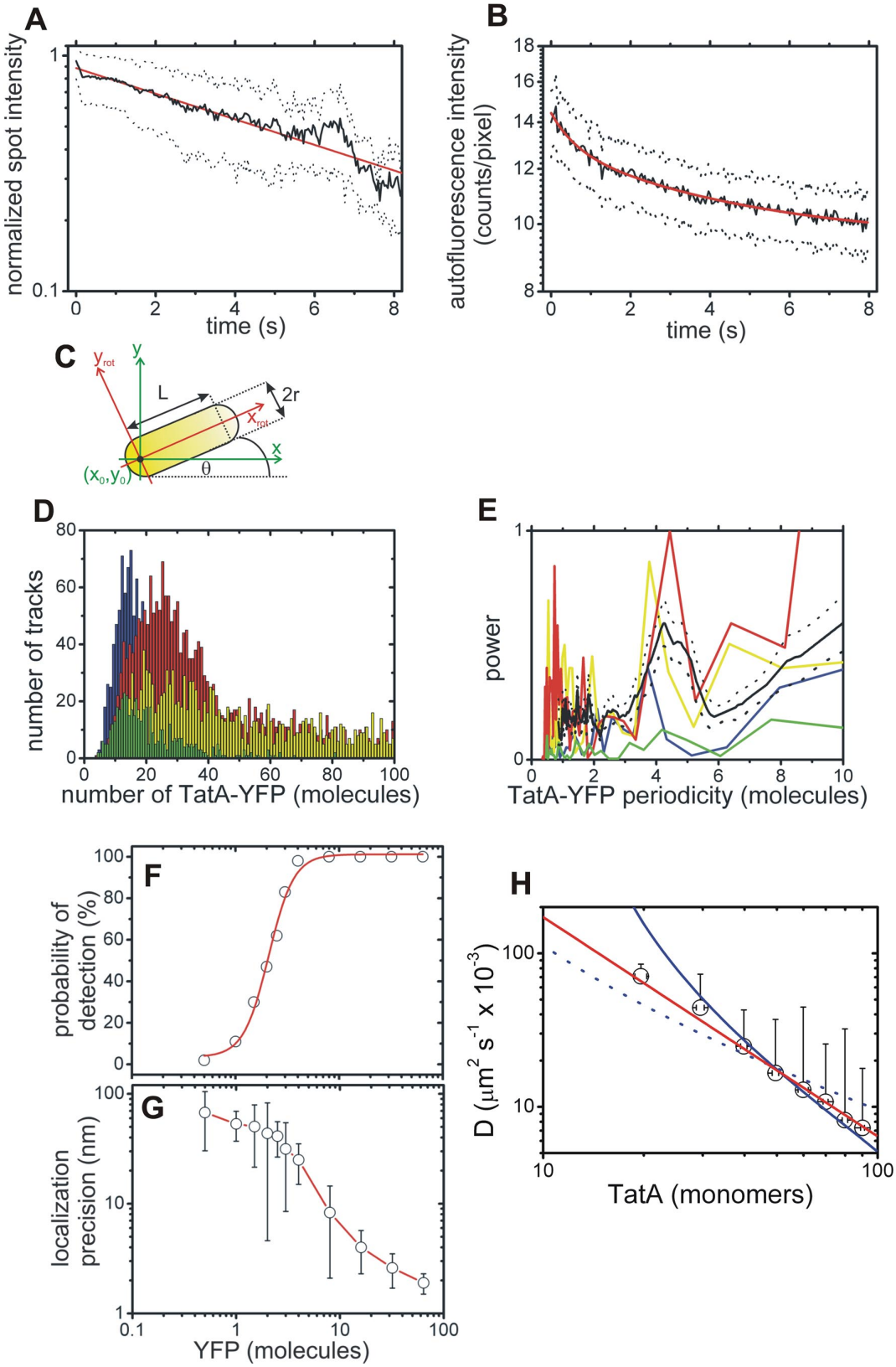

Fig. S1. (*A* and *B*) Average bleach curves (solid black lines) on semilog plots for spot intensity (*A*) and autofluorescence (*B*). SD error bounds (dotted black lines) and exponential fits (red) are shown. (*C*) Schematic of a bacterial cell (yellow) illustrating the orientation of the Cartesian camera axes (*xy*, green) relative to the rotated Cartesian axes ($x_{rot}y_{rot}$, red). (*D*) Stoichiometry for four example cultures. (*E*) Power spectrum of the pairwise difference distribution for each histogram of *D*, using the same color-coding, mean spectrum from all 10 different cultures used with dotted SD error-bounds in black. (*F* and *G*) Variation of detection probability (*F*) (sigmoidal fit in red) and localization precision (*G*), with number of simulated YFP molecules per spot (SD error bars). (*H*) Fitting the diffusion data using a Saffman-Delbrück approach for a ring (blue, solid line) and disk (blue, dotted line) model, compared with the straight-line fit on the log-log plot (red line) of gradient -1.2 ± 0.4 consistent with the heuristic $1/r$ ring model.

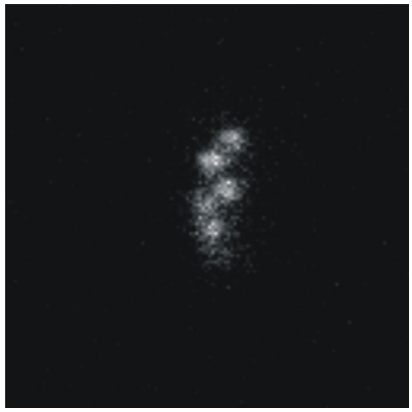

Movie S1. Movie of strain AyBC observed under continuous epifluorescence illumination, sampled at 25 Hz and displayed at normal speed.

Movie S1

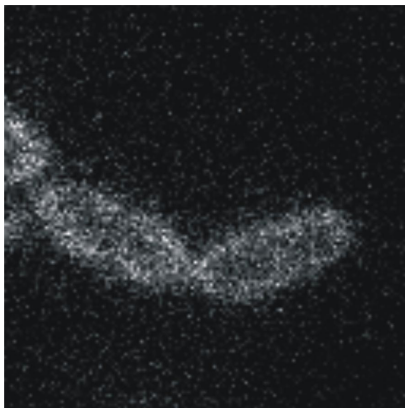

Movie S2. Movie of strain Ay observed under continuous epifluorescence illumination, sampled at 25 Hz and displayed at normal speed.

Movie S2

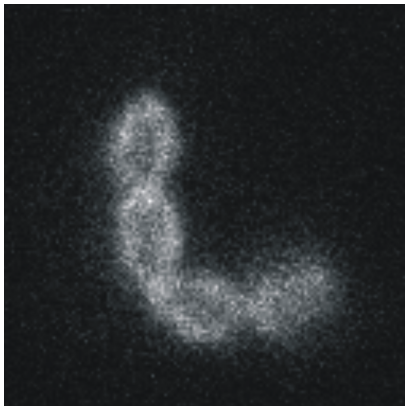

Movie S3. Movie of strain AyC observed under continuous epifluorescence illumination, sampled at 25 Hz and displayed at normal speed.

Movie S3

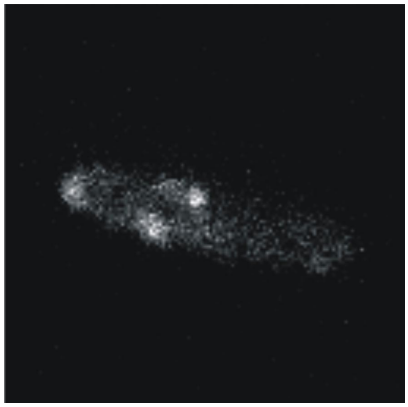

Movie S4. Movie of strain Ay expressing *tatBC* under the control of an arabinose-inducible promoter. The cells were observed under continuous epifluorescence illumination, sampled at 25 Hz and displayed at normal speed.

Movie S4

Table S1. Tat phenotypes of strains used in this study

Strain	*tat* genotype	SDS growth	TMAO growth	Periplasmic TMAO reductase, μmol·min^{-1} (mg protein)$^{-1}$
ABC (WT)	*tatABCDE*$^{+}$	+++	+++	1.10
BC	Δ*tatA*Δ*tatE*, *tatBCD*$^{+}$	–	–	0.10
AAyBC	*tatABCDE*$^{+}$, *tatA-eyfp*$^{+}$	+++	+++	1.24
AyBC	Δ*tatA*Δ*tatE*, *tatBCD*$^{+}$, *tatA-eyfp*$^{+}$	+++	+++	0.13

SDS growth refers to culture on LB agar plates containing 2% SDS. TMAO growth refers to culture under anoxic conditions on minimal medium agar plates containing glycerol as carbon source and trimethylamine *N*-oxide as respiratory electron acceptor. the growth experiments were carried out as described in ref. 1. Determination of periplasmic TMAO reductase activity was as described in ref. 1.

Table S2. Estimation of cellular TatA-YFP content

Strain	Molecules/spot*	Molecules/cell, all spots	Molecules/cell, *ex* spots	Total molecules/cell	$D/\mu m^2\ s^{-1} \times 10^{-3}$
AyBC	25 (0.3)	360 (4)	105 (3)	462 (16)	43 (1)
AyBC + FCCP	24 (0.4)	340 (6)	58 (3)	393 (21)	46 (1)
AyC	-	-	680 (72)	680 (72)	
Ay	-	-	653 (21)	653 (21)	118 (4)†
Ay + pBC	15 (0.5)	160 (5)	561 (13)	717 (30)	51 (3)

*Median (standard error), otherwise quoted as mean (standard error).
†From tracking following FRAP.